Article

Impact Performance of 3D Orthogonal Woven Composites: A Finite Element Study on Structural Parameters

Wang Xu [1,*], Mohammed Zikry [2] and Abdel-Fattah M. Seyam [1,*]

[1] Wilson College of Textiles, North Carolina State University, Raleigh, NC 27695, USA
[2] Department of Mechanical and Aerospace Engineering, North Carolina State University, Raleigh, NC 27695, USA; zikry@ncsu.edu
[*] Correspondence: wxu8@ncsu.edu (W.X.); aseyam@ncsu.edu (A.-F.M.S.)

Abstract: This study uses the finite element method (FEM) to investigate the effect of key structural parameters on the impact resistance of E-glass 3D orthogonal woven (3DOW) composites subjected to low-velocity impact. These structural parameters include the number of y-yarn layers, the path of the binder yarn (z-yarn), and the density of the x-yarn. Using ABAQUS, yarn-level finite element (FE) models are created based on the measured geometrical parameters and validated for energy absorption and damage behavior from experimental data gathered from the previous study. The results from finite element analysis (FEA) indicate that the x-yarn density and the binder path substantially influenced the composites' damage behavior and impact performance. Increasing x-yarn density in 3DOW leads to a 15% increase in energy absorption compared to models with reduced x-yarn densities. Moreover, as the x-yarn density increases, crack lengths at the back face of the resin matrix decrease in the y-yarn direction but increase in the x-yarn direction. The basket weave structure absorbs less energy than plain and 2×1 twill structures due to the less constrained weft primary yarns. These results underscore the importance of these structural parameters in optimizing 3DOW composite for better impact performance, providing valuable insights for the design of advanced composite structures.

Keywords: finite element analysis; damage mechanics; low-velocity impact; 3D woven composite

1. Introduction

Three-dimensional (3D) woven composites have attracted significant interest in recent years due to their exceptional mechanical properties and broad applicability, such as aerospace and automotive systems and ballistic protection [1–3]. These composites are characterized by reinforcing fibers woven in three-dimensional structures, offering improved out-of-plane properties and delamination resistance compared to traditional 3D woven preforms made from a stack of 2D woven composites [4,5]. The 3D woven composites show enhanced impact resistance and straightforward and economical production of complex shapes with structural integrity compared to their 2D counterparts [6,7]. The 3D orthogonal woven composites (3DOW) further capitalize on the benefits of 3D weaving by introducing a third set of yarns (binder or z-yarns) in the through-thickness direction [8–11]. In 3DOW structures, there is no interlacement between x- and y-yarns and thus no crimp [12–14]. The binder yarns combine the y- and x-layers by traveling from the top to the bottom layers of the 3DOW in the z-direction.

Several experimental and finite element studies have been conducted in the past to investigate the role of binder yarn on the mechanical properties or impact performance of 3DOW composites [7,15–18]. Zhang et al. [19] studied the binder yarn's role under both quasi-static and high-strain-rate compressive loading conditions. They found that the binder yarn significantly influenced in-plane responses during the compressive deformation and failure modes of 3DOW composites. Similarly, Luo et al. [20] studied the

transverse impact behavior of the hybrid 3DOW subjected to quasi-static and transverse impact in y- and x-directions and they concluded that there was no delamination observed due to the existence of the binder yarns in the 3DOW structure. Baucom and Zikry [21,22] studied damage progression in 2D and 3DOW woven E-glass composite systems under various impact velocities using finite element methods. They reported that the z-yarns contribute to more energy absorption in 3DOW composites than in 2D composites by activating new mechanisms like surface x-yarns pulled through unbroken crimp of the binder yarns. Characterization methods were also used to examine the effect of the binder yarns in 3DOW composites under impact. Seltzer et al. [5] found that the 3D woven composite could dissipate over twice the energy than the 2D laminate, irrespective of their characteristics. Further X-ray microtomography revealed that the introduction of the binder yarns delayed delamination and maintained the structural integrity of 3D composites. Castaneda et al. [6,23] employed Digital Image Correlation (DIC), Acoustic Emission, and micro-CT to evaluate both global and local strain patterns to track the damage process of 3DOW composite under uniaxial tensile loading and fatigue experiments. The main role of the binder yarn was found to be associated with transverse reinforcement, coupled with significant out-of-plane effects. Hart et al. [6] characterized the damage of both plate and beam samples of 2D and 3DOW composites with the same areal density by high-resolution cross-sectional images after impact. Their results indicated that the binder yarn of the 3D structure provided suppression of delamination propagation and opening, which led to a shorter delamination length and the opening of 3DOW after impact. Hart et al. [24] further compared the post-impact response of 2D and 3DOW composite plates and beams by Compression-after-impact and Flexure-after-impact tests. Normalized residual strength and stiffness for compression and flexure were compared. The results showed that the through-thickness binder yarn helps 3DOW composite retain greater post-impact mechanical performance. Midani et al. [25] investigated the effect of the binder yarn component on the mechanical properties of 3DOW composite by drop-weight impact. The results showed that the z-yarn played a significant role in maintaining the orientation, alignment, and spacing of the y- and x-yarns. Ghosh and De [26] simulated the role of the binder yarn of the 3DOW under high-velocity impact. The meso-level model showed that the binder-yarn reinforcement confined fiber tensile damage by guiding the stress waves through them but the binder yarns were unable to arrest matrix shear damage efficiently. Miao et al. [15] assessed the damage resistance of a layered unidirectional, layered woven, and 3DOW composite under low-velocity impact. The roles of the binder yarn were identified as cracking triggers due to the weak debonding with resin around it. Moreover, the resin damage initiated on the bottom surface of the composite grew along the binder yarn in the through-thickness direction then developed horizontally and blocked by the binder yarn, which avoids the formation of delamination. Dai et al. [27] investigated the tensile, compressive, and flexural performance of four orthogonal woven composites with different binder yarn paths. They reported that the change in the binder yarn path affected the mechanical performance by altering the distribution of resin-rich regions and the waviness of the load-carrying fibers. In addition, the binding points served as the damage initiation sites within the resin-rich area and the long distance between two adjacent binding points in the orthogonal structure led to longer delamination length. Dash and Behera [28] investigate the tensile, impact, and knife penetration performance of 3DOW fabrics with three different binder yarn paths. Plain weave, 4x4 twill, and 4 × 4 basket were selected. The number of cross-over points in a particular area of the structure was found to be closely related to the impact energy absorption.

Another critical factor that influences the mechanical and impact performance of 3DOW composites is the x-yarn density. Several experimental and finite element studies have been conducted to investigate the effect of weave or x-yarn density on the mechanical properties or impact performance of 3D woven composites. Sun et al. [29] characterized the damage morphology of 3DOW after low-velocity impact by X-ray micro-computed tomography and found that the impact damage has significant directionality determined

by the weft/warp orientation of the composites. Further finite element analysis revealed that the x-/y-yarns play an important role in absorbing energy at the beginning of the impact. Nasrun et al. [30] investigated the influence of x-yarn density on the tensile strength of 3D angle interlock woven fabric. Samples with four different x-yarn densities were manufactured, and it was found that increasing x-yarn density would improve the tensile strength of the sample. Li et al. [31] used the finite element method to predict the mechanical properties of 3D angle interlock woven composites with different structural parameters and revealed the relationship between x-yarn density and Young's modulus. Hamouda et al. [32] carried out flexural and tensile tests on 3DOW composite with low and high x-yarn densities and the effect was evaluated using the General Linear Model. The statistical analysis showed that x-yarn density had a significant effect on the bending strength, flexural modulus, flexural strength, and tensile strength of 3DOW composites. Neale et al. [33] investigated the effect of x-yarn density on the mechanical behavior of 3DOW composites under three-point bending, quasit-static and dynamic impacts. The results showed that increasing the yarn density generally decreased the specific energy absorption rate, but the energy absorption, compression and bending properties were improved by 19%, 18% and 72%, respectively. This study demonstrated that small changes in the x-direction yarn density (transverse) and weave structure can significantly improve the y-direction (axial) energy absorption without fundamentally redesigning the weave structure. Midani et al. [34] evaluated the effect of the structural parameters on the impact behavior of 3DOW composites under Izod, Tup, and Charpy impacts. Although the effect on the total penetration energy was not as significant as increasing the number of layers because the amount of fibers added by increasing the yarn density was much smaller than that added by increasing the number of layers, the change in x-yarn density still had a significant effect on the total energy absorption.

Although numerous studies have investigated the role of binder yarn path configuration in 3DOW composites, most have restricted their focus to a single configuration. A comprehensive analysis across varying yarn paths on impact performance is absent. While some experimental research has studied the influence of different binder yarn paths, the detailed numerical exploration of these effects remains limited. Moreover, the impact of x-yarn density on 3DOW performance has predominantly been explored through experimental studies, leaving a gap in detailed numerical simulations that could offer more information. These gaps underscore the urgency of delving deeper into the structural parameters' effects on the impact response of 3DOW composites, particularly through finite element analysis which could offer more details that cannot be obtained in experimental study. Doing so will enable the development of guidelines for customizing the structural parameters of 3DOW composites to achieve optimal impact performance for specific applications, particularly those demanding improved impact performance.

In this paper, we aim to numerically study the impact of x-yarn density and binder yarn path. We have conducted an in-depth finite element analysis to uncover the dynamic damage behavior of E-glass 3DOW reinforced composites under low-velocity impact. The 3DOW models were developed based on the measured geometric parameters and experimental results provided by Midani et al. [34]. We utilized ABAQUS/Explicit user-defined subroutine (VUMAT) based on MAT162 [35], a progressive composite damage model, to simulate the damage behavior of resin-impregnated E-glass fiber. The damage model of the resin matrix was designed to incorporate ductile behavior with isotropic characteristics. Our yarn-level FE model was validated with experimental results, enabling further characterization of damage evolution. Our simulation results not only delineate how structural parameters influence damage resistance but also illustrate how these parameters can be manipulated to optimize 3DOW composites for enhanced impact performance, offering robust guidelines for future material design.

2. Finite Element Model

2.1. Geometric Model

Midani et al. [34] manufactured 3DOW composite samples with fixed y-yarn density and three different binder yarn weave structures (plain weave, 2×2 basket, and 2×2 twill) and three different x-yarn (weft) densities (4.87, 5.45, and 5.87 picks/cm/layer). They performed tensile and drop weight impact tests to investigate the influence of x-yarn density and binder yarn path on the mechanical performance of 3DOW composites. Based on their experimental results, 11 finite element models were created to study the effect of structural parameters on the impact resistance of 3DOW, as detailed in Table 1. The thickness of the model is based on the average measured dimension of the reinforcements in the 3DOW samples, which is constant across the models with different numbers of layers.

Table 1. Specifications of 3DOW models.

Model Name	x-Yarn Density/Layer (cm^{-1})	Binder Yarn Path	y-Yarn Density/Layer (cm^{-1})	Number of Layers	Model Thickness (mm)	Sample Thickness (mm)
2L487	4.87	Plain	2.36	2	2.19	2.19
2L487twill	4.87	Twill	2.36	2	2.19	2.47
2L487basket	4.87	Basket	2.36	2	2.19	2.53
2L545	5.45	Plain	2.36	2	2.19	2.09
2L587	5.87	Plain	2.36	2	2.19	2.20
3L487	4.87	Plain	2.36	3	2.95	3.05
3L545	5.45	Plain	2.36	3	2.95	3.18
3L587	5.87	Plain	2.36	3	2.95	3.22
4L487	4.87	Plain	2.36	4	3.71	3.59
4L545	5.45	Plain	2.36	4	3.71	3.57
4L587	5.87	Plain	2.36	4	3.71	3.69

To efficiently simulate the impact resistance of 3DOW composites, a yarn-level model (30 mm $\times$ 30 mm) was developed to understand the impact of structural parameters on the impact resistance of 3DOW. This dimension corresponds to one-quarter of the full-size experimental samples, which measure 60 mm $\times$ 60 mm. X- and Y-symmetry are attributed to the corresponding surfaces in ABAQUS to ensure an accurate representation of the weave pattern and mat of the composite. Figure 1 depicts the numerical model consisting of a rigid striker and a yarn-level 3DOW composite plate. As shown in Figure 1, the yarn-level models of x- (weft), y- (warp), and binder yarns were assembled with the resin matrix to construct the 3DOW composite plate. The impact energy was assigned to the rigid striker by setting the initial velocity (4.4 m/s) and inertial mass (22.67 kg), resulting in an impact energy of approximately 219 J. The composite plate material system comprised the resin matrix and three types of impregnated yarns (x-, y-, and z-yarns). The x- and y-reinforcement geometric models were assumed to be straight without crimp, and the binder yarn path was simplified to a W shape (as shown in Figure 1). The cross-sectional shapes of all yarns were assumed to be rectangular with measured dimensions. The resin matrix and 3DOW preform geometric models were assembled in ABAQUS, and a "Tie constraint" was used to define the interactions between them [36]. A tie constraint in ABAQUS ties two surfaces together to ensure there is no relative motion between the connected parts, even if the meshes of the connected surface do not match.
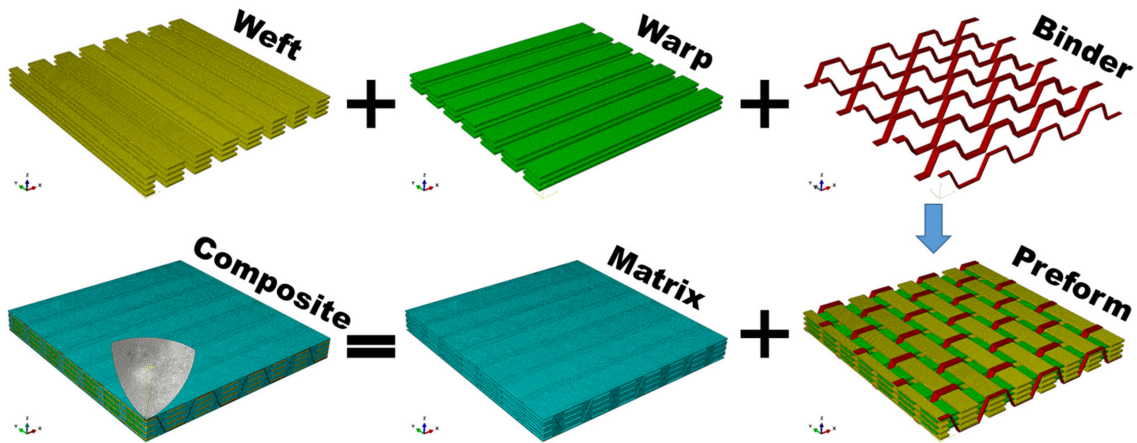
Figure 1. Finite element model of 3DOW composite.

The reinforcement models were meshed using eight-node solid elements (C3D8R in ABAQUS notation), while a combination of six-node solid elements (C3D6 in ABAQUS notation) and C3D8R elements was employed to mesh the matrix. A mesh convergence analysis was conducted and is detailed in Figure 2. In this analysis, models of varying mesh sizes in the range of 0.10 mm–0.25 mm were compared based on their residual velocities as a function of time. The number of elements (blue bars in Figure 2) decreased from 2,014,524 to 281,972 as mesh sizes increased, substantially reducing the calculation time from approximately 250 h to 23 h (red bars in Figure 2). Moreover, for mesh sizes of 0.175 mm and 0.135 mm, the calculation time increased significantly, but residual velocities had negligible changes. Conversely, reducing the element size from 0.21 mm to 0.175 mm yielded the opposite results, as indicated by Figure 2. Therefore, the mesh group with an element size of 0.175 mm with C3D8R and C3D6 was selected for this study.
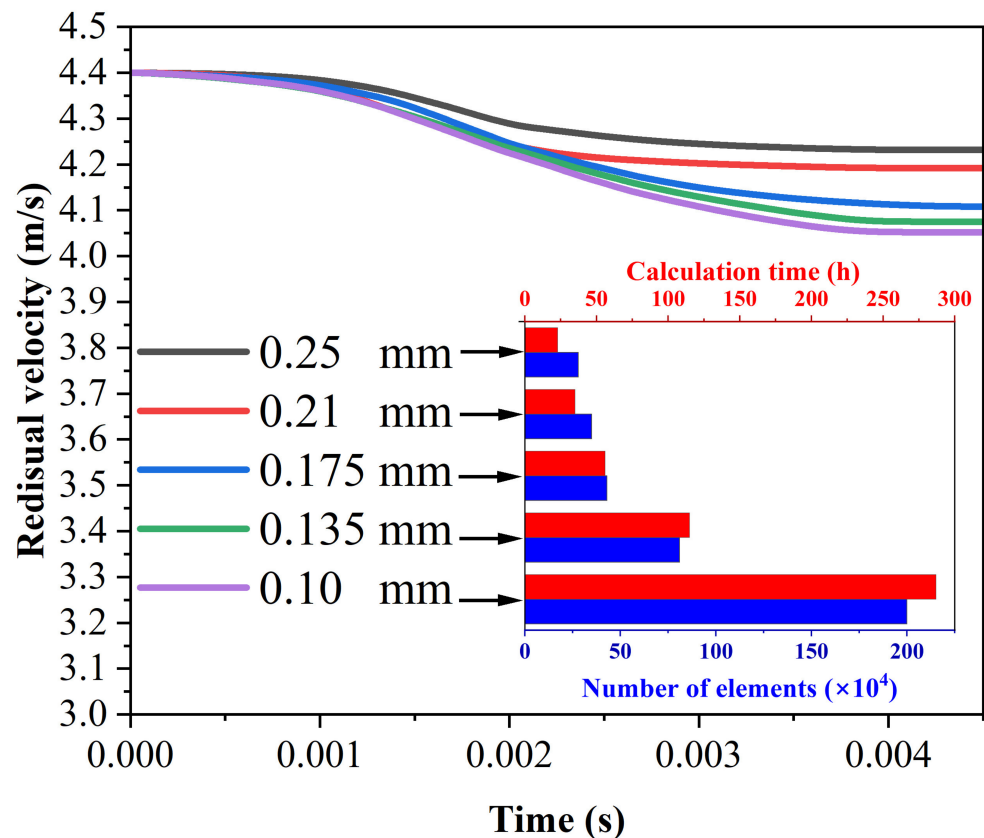

Figure 2. Mesh sensitivity study for 3DOW composite.

2.2. Damage Model

The resin matrix was set as an isotropic material exhibiting elastic–plastic characteristics following the J2 isotropic plastic hardening theory. The mechanical properties of the resin matrix are listed in Tables 2 and 3.

Table 2. Mechanical properties of resin matrix [19].

Resin	Properties
Modulus E (MPa)	2100
Shear modulus G (MPa)	808
Tensile strength (MPa)	115
Compressive strength (MPa)	146
Density (g/mm^3)	0.0013
Poisson's ratio	0.33
Fracture strain	0.057

Table 3. Plastic parameters of the resin matrix.

Yield Stress (MPa)	Plastic Strain (%)
25	0
33	0.30
82.64	0.78
118.46	1.30
142.50	2.39
159.52	3.00
169.60	3.16
181.70	3.79
188.83	4.43
185.70	5.05
192.71	5.69

MAT162 is a continuum damage mechanic model for fiber-reinforced composite and it has been widely used to predict the behavior of textile composite under impact [37–40]. It consists of six failure modes for unidirectional composites. Since the delamination mode can only be applied when pre-defined interface layers are modeled, this study did not consider it. For the fiber crush mode, Sridharan and Pankow [41] reported that incorporating the fiber crush failure led to higher energy absorption and delayed damage formation. Consequently, the fiber crush failure was suppressed in this study. The damage initiation criteria for the five failure modes—fiber tension–shear, fiber compression, fiber crush through the thickness, transverse compression matrix, and perpendicular shear matrix—derived from MAT162 are described in Equations (1)–(5).

Fiber tension–shear:

$$\left(\frac{E_a\langle -\varepsilon_a\rangle}{X_T}\right)^2 + \left(\frac{G_{ab}^2\varepsilon_{ab}^2 + G_{ca}^2\varepsilon_{ca}^2}{X_{FS}^2}\right) - r_1^2 = 0 \tag{1}$$

Fiber compression:

$$\left(\frac{E_a\langle -\varepsilon_a'\rangle}{X_C}\right)^2 - r_2^2 = 0 \tag{2}$$

Fiber crush through thickness:

$$\left(\frac{E_c\langle -\varepsilon_c\rangle}{S_{FC}}\right)^2 - r_3^2 = 0 \tag{3}$$

Transverse compression matrix:

$$\left(\frac{E_b \langle -\varepsilon_b \rangle}{Y_c}\right)^2 - r_4^2 = 0 \tag{4}$$

Perpendicular shear matrix:

$$\left(\frac{E_b \langle \varepsilon_b \rangle}{Y_T}\right)^2 + \left(\frac{G_{bc}\varepsilon_{bc}}{S_{bc} + S_{SRC}}\right)^2 + \left(\frac{G_{ab}\varepsilon_{ab}}{S_{ab} + S_{SRB}}\right)^2 - r_5^2 = 0 \tag{5}$$

where E_i and G_{ij} represent elastic and shear moduli, ε_i are the strain components of the element, X_T, X_c, Y_T, and Y_C are the longitudinal and transverse tensile and compressive strengths, S_{ij} is the shear strengths, and r_j is the failure index used to calculate damage progression factors.

Regarding the damage to the impregnated yarn, we employed a VUMAT based on a modified MAT162 to simulate damage initiation and progression. Figure 3 illustrates the calculation procedure for damage detection, progression, and deletion of the damaged element. The three-dimensional stresses were used to calculate strain and detect damage initiation for various damage modes (Equations (1)–(5)). Upon detecting damage, the corresponding damage progression factors were calculated and used to degrade the stiffness matrix and consequently the stress. At the end of each increment, the computed results were assessed according to element deletion rules, as depicted in Figure 3, to determine any necessary element deletions.
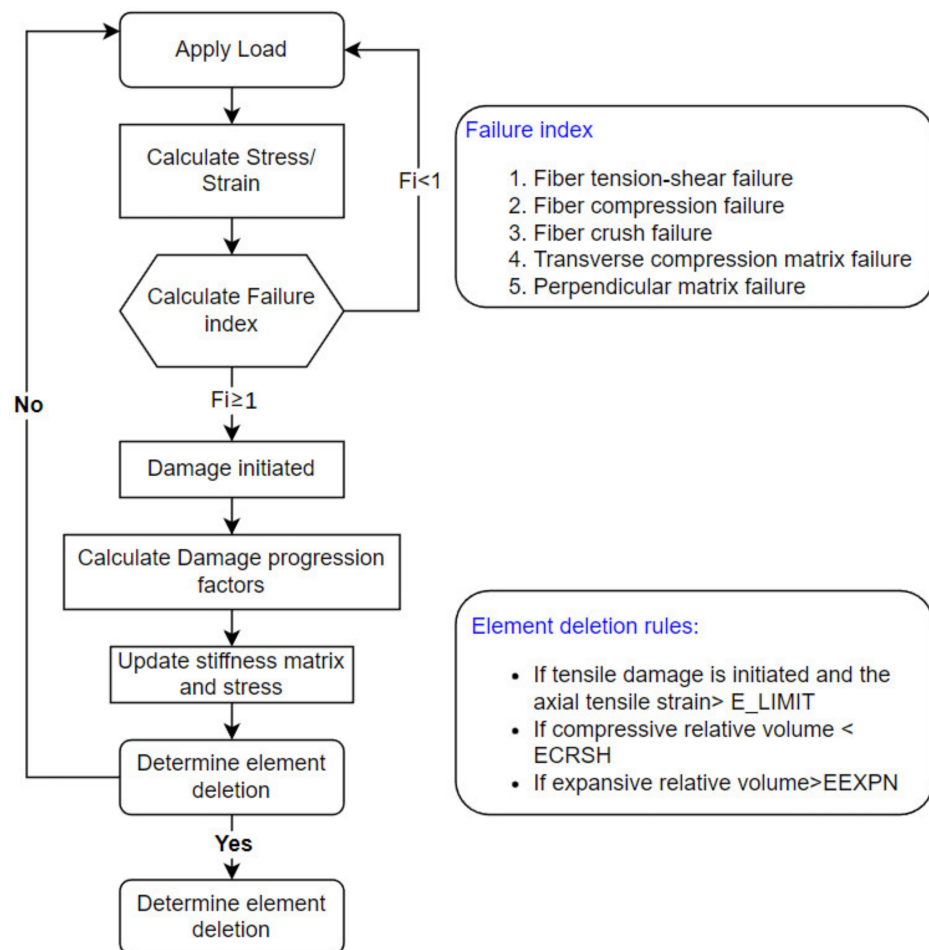

Figure 3. Logic Flow of deformation, damage initiation, damage progression, and element deletion in VUMAT.

Once an element is marked as damaged, damage variables were calculated by coupling the collected quantity of damage with the damage coupling matrix to represent the damage propagation for each damage mode using Equation (6).

$$\omega_i = \max\left\{ \left(1 - \exp\left(\frac{1}{m_j}(1 - r_j^{m_j}) \right) \right) * q_{ij} \right\} \tag{6}$$

ω_i is the growth rate of damage variables, m_j is the material softening parameters, q_{ij} is the damage coupling matrix defined in Equation (7).

$$\left[q_{ij} \right] = \begin{bmatrix} 1 & 1 & 1 & 0 & 0 \\ 0 & 0 & 1 & 1 & 1 \\ 0 & 0 & 1 & 0 & 0 \\ 1 & 1 & 1 & 1 & 1 \\ 0 & 0 & 1 & 1 & 1 \\ 0 & 0 & 1 & 0 & 0 \end{bmatrix} i = 1, \ldots, 6; j = 1, \ldots, 5. \tag{7}$$

Damage variables are then used to degrade the components of the compliance matrix [S], as shown in Equation (2). The stress components were updated using the degraded compliance matrix (Equation (8)).

$$[S] = \begin{bmatrix} \frac{1}{(1-\omega_1)E_1} & S12 & S13 & 0 & 0 & 0 \\ S21 & \frac{1}{(1-\omega_2)E_2} & S23 & 0 & 0 & 0 \\ S31 & S32 & \frac{1}{(1-\omega_3)E_3} & 0 & 0 & 0 \\ 0 & 0 & 0 & \frac{1}{(1-\omega_4)G_{12}} & 0 & 0 \\ 0 & 0 & 0 & 0 & \frac{1}{(1-\omega_5)G_{23}} & 0 \\ 0 & 0 & 0 & 0 & 0 & \frac{1}{(1-\omega_6)G_{31}} \end{bmatrix} \tag{8}$$

When an element failed, it was deleted if any of the three following conditions were met: (1) fiber tensile damage is initiated and the axial tensile strain of the element exceeded the failure strain (E_LIMIT), (2) if the ratio of current volume to initial volume in a failed element was lower than the minimum limit (ECRSH), and (3) if the expansive relative volume of a failed element was larger than the maximum limit (EEXPN). Table 4 shows the input material properties of the resin-impregnated E-glass fibers.

Table 4. Material properties of impregnated E-glass fiber in 3DOW.

Property	Symbol	Value (Units)
Density	ρ0	0.002 (g/mm^3)
Young's modulus in direction 1	E1	45,000 (MPa)
Young's modulus in direction 2	E2	10,000 (MPa)
Young's modulus in direction 3	E3	10,000 (MPa)
Poisson's ratio in direction 21	ν12	0.31
Poisson's ratio in direction 31	ν13	0.31
Poisson's ratio in direction 32	ν32	0.41
Shear modulus in direction 12	G12	3000 (MPa) [42]
Shear modulus in direction 31	G13	3000 (MPa) [42]
Shear modulus in direction 32	G23	2300 (MPa) [42]
Longitudinal tensile strength in direction 1	XT	2200 (MPa) 107 [16]
Longitudinal compressive strength in direction 1	XC	1980 (MPa) [16]
Transverse tensile strength in direction 2	YT	100 (MPa) [15]
Transverse compressive strength in direction 2	YC	256 (MPa) [15]
Matrix mode shear strength in direction 12/13	S12/S13	113 (MPa) [15]

Table 4. *Cont.*

Property	Symbol	Value (Units)
Matrix mode shear strength in direction 23	S23	98 (MPa) [15]
Crush strength in direction 3	SFC	185,000 (MPa)
Fiber mode shear strength	SFS	350 (MPa)
Residual compressive strength factor	SFFC	0.1 [39]
Coulomb friction angle	PhiC	0.17 (rad) [43]
Limiting damage factor	OMGMX	0.999 [43]
Eroding axial strain	E_LIMIT	0.05 [44]
Eroding compressive volume strain	ECRSH	0.001 [43]
Eroding volumetric strain	EEXPN	4.5 [43]
Coefficient of strain rate fiber strength properties	Crate1	0.03 [43]
Coefficient of strain rate for axial moduli	Crate2	0.00 [43]
Coefficient of strain rate for shear moduli	Crate3	0.03 [43]
Coefficient of strain rate for transverse moduli	Crate4	0.03 [43]
Coefficient of softening for axial fiber damage	am1	100 [43]
Coefficient of softening for transverse fiber damage	am2	10 [43]
Coefficient of softening for crush damage	am3	0.5 [43]
Coefficient of softening for matrix failure	am4	0.2 [43]

3. Results and Discussion

3.1. Validation

To validate the accuracy and effectiveness of the finite element model, various numerical results were compared with previous experimental findings [34]. Global responses of the load–time curve of 2-layer 3DOW models with different x-yarn densities and binder yarn paths were compared with the best-matching examples, as illustrated in Figures 4 and 5. In general, the predicted loads from FEA at the beginning of the impact process were greater than measured loads (EXP). Subsequently, peak loads reached about the same time. A notable difference occurred when the curves from the numerical analysis smoothly approached zero, while the experimental load remained constant for a short time before plummeting abruptly to near zero and then recovering slightly before reaching zero, as shown in both Figures 4 and 5. The finite element model slightly underestimates the duration of the impact, but it still shows a good agreement with the experimental results.
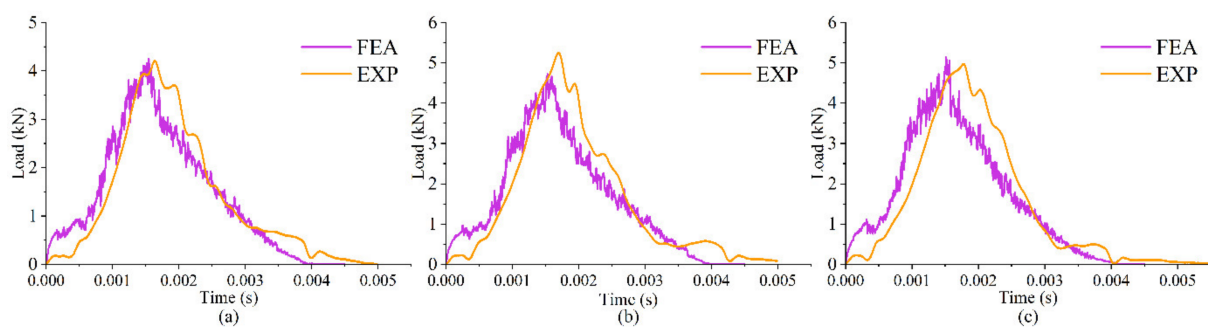

Figure 4. Experimental and numerical load–time curve comparison for (**a**) 2L487, (**b**) 2L545, and (**c**) 2L587.
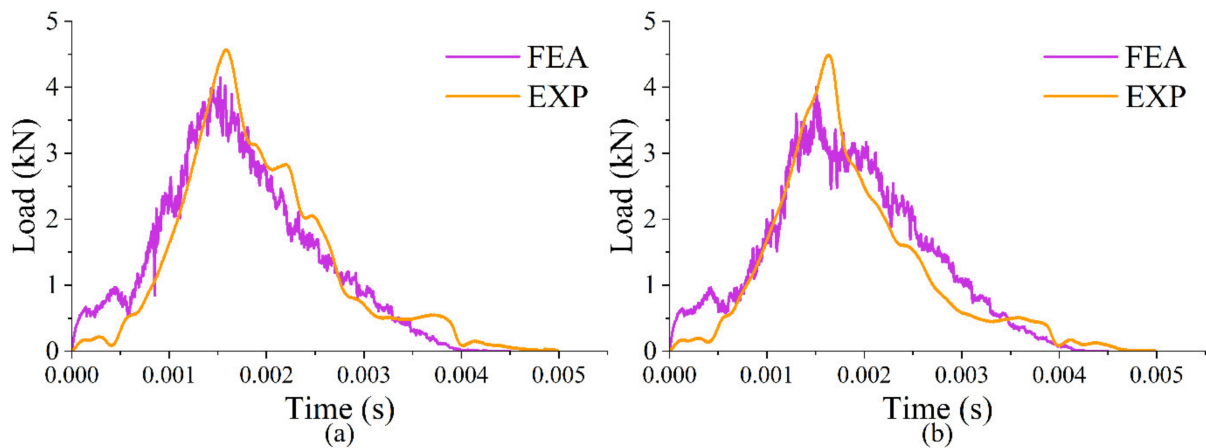
Figure 5. Experimental and numerical load–time curve comparison for (**a**) 2LTwill and (**b**) 2LBasket.

Table 5 compares the energy absorption of simulations and tests, normalized by thickness, total areal density, and preform areal density. The maximum differences were 15.16% for energy normalized by thickness, 15.49% for energy normalized by areal density, and 11.52% for energy normalized by preform areal density. The comparison of normalized energy absorption supports the reliability of the numerical model for this study.

Table 5. Numerical and experimental energy absorption comparison.

Model	Energy/Thickness (J/mm)		Error (%)	Energy/Areal Density (kJ/g/mm^2)		Error (%)	Energy/Preform Areal Density (kJ/g/mm^2)		Error (%)
	Exp	FEA		Exp	FEA		Exp	FEA	
2L487	13.67	12.61	7.77	8.92	7.97	12.22	18.87	17.89	5.48
2L545	13.03	13.67	−4.91	8.60	8.51	0.96	18.50	17.95	3.04
2L587	13.80	14.52	−5.22	9.39	9.04	5.29	19.29	17.47	10.44
2LTwill	13.34	11.95	9.97	8.60	7.65	12.07	16.86	17.32	−2.62
2LBasket	13.53	12.15	10.13	8.70	7.51	15.49	18.40	17.00	8.28
3L487	16.21	16.0	1.29	10.65	10.15	5.05	21.74	21.84	−0.45
3L545	16.08	17.56	9.20	10.62	10.77	−1.31	21.85	20.95	4.30
3L587	17.68	18.05	2.09	11.28	11.09	1.81	21.95	21.62	1.53
4L487	20.31	17.23	15.16	13.02	10.90	11.51	27.41	22.92	11.52
4L545	21.25	19.25	12.19	12.22	11.87	3.04	26.45	23.56	12.28
4L587	21.23	20.02	5.69	12.35	12.26	0.88	23.98	23.43	2.35

3.2. Effect of x-Yarn Density

The predicted energy absorption for 3DOW models with different x-yarn yarn densities is demonstrated in Figure 6. As shown in Figure 6, energy absorption increased with increasing weft yarn densities in 2-layer, 3-layer, and 4-layer models. Increasing the number of layers also enhanced the effect of increased x-yarn density on energy absorption, although this effect diminished with increasing x-yarn density. The greatest improvement occurred in 4-layer models, where a 15.6% increase in energy absorption was achieved when the x-yarn density increased from 4.87 to 5.87 picks/cm/layer, as indicated in Figure 6.
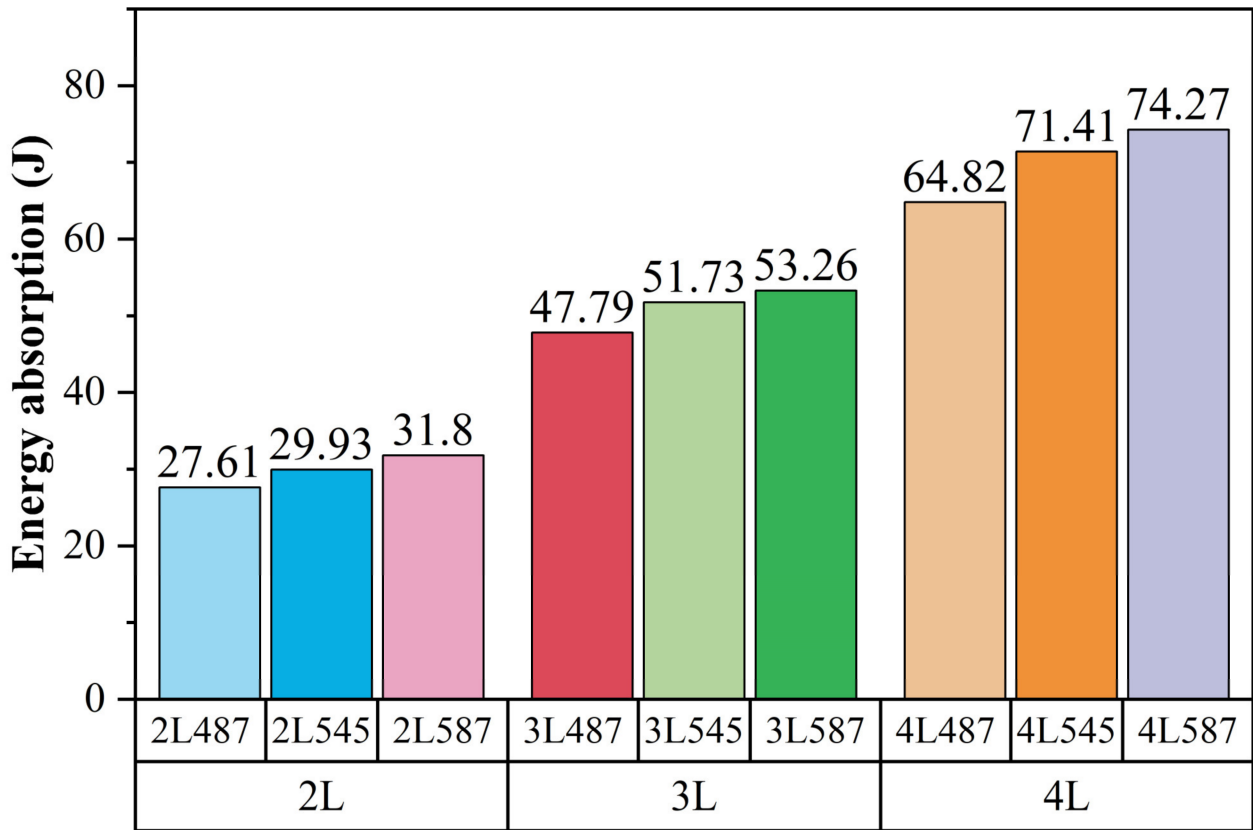
Figure 6. Energy absorption comparison from finite element analysis in 2-, 3-, and 4-layer 3DOW with varying x-yarn densities.

When a striker impacts a composite plate, longitudinal and transverse waves are immediately generated, which are the primary means of dissipating energy [45]. The transverse deflection at impact initiation generates bending waves, which have been demonstrated to be an important method of impact energy dissipation. To further analyze energy absorption distributions in 3DOW models, y- and x-reinforcements were categorized according to contact modes into primary and secondary yarns, facilitating energy distribution during the impact event. Binder yarns were excluded from the energy absorption comparison because the energy absorbed by binder yarns was substantially less than that of y- and x-yarns. Warp and weft reinforcements in direct contact with the strikers were classified as warp primary yarns (YP) and weft primary yarns (XP), while the rest of the reinforcements were classified as warp secondary yarns (YS) and weft secondary yarns (XS). The FEA energy absorption distribution in terms of x-yarn density at different numbers of y-yarn layers is shown in Figure 7a–c.

In the FE simulation of impact, the kinetic energy carried by the striker is mainly absorbed by three mechanisms: internal energy (IE), kinetic energy (KE), and frictional dissipated energy (FD) [46]. It was found that the majority of the striker's kinetic energy was converted to internal energy (IE) in this study. Figure 7a depicts how increasing the x-yarn density facilitates the weft secondary yarns and warp primary yarns to absorb and store more impact energy as internal energy. The XP of both 2L545 and 2L587 was approximately 1J greater than that of 2L487, but the IE absorption decreased slightly as the x-yarn density increased from 5.45 to 5.87 picks/cm. As shown in Figure 7b, the increase in IE with an increase in x-yarn density from 5.45 to 5.87 picks/cm was not as significant for 3-layer 3DOW as the difference between 3L487 and 3L545. However, IE in the weft primary yarns increased as x-yarn density increased. Similar to the 2-layer 3DOW, the IE absorption of the warp primary yarns and the weft secondary yarns increased as the x-yarn density increased. As shown in Figure 7c, the same trend can be observed in

the 4-layer 3DOW models, where the IE absorption in x-yarns and warp primary yarns increases with an increase in x-yarn density. However, as x-yarn density increased from 5.45 to 5.87 picks/cm, the difference in IE absorption in x-yarns diminished. As for warp secondary yarns, IE absorption appeared to have a minimal correlation with x-yarn density variations regardless of the number of y-yarn layers. Variations in the internal energy of x-yarns and warp primary yarns resulting from changes in x-yarn density account for the majority of the difference in energy absorption in 3DOW. Thus, it can be deduced that an increase in x-yarn density will likely result in greater energy absorption. This is because models with greater x-yarn density have greater fiber volume fractions, which means more fibers can absorb the impact, resulting in larger IE absorption.
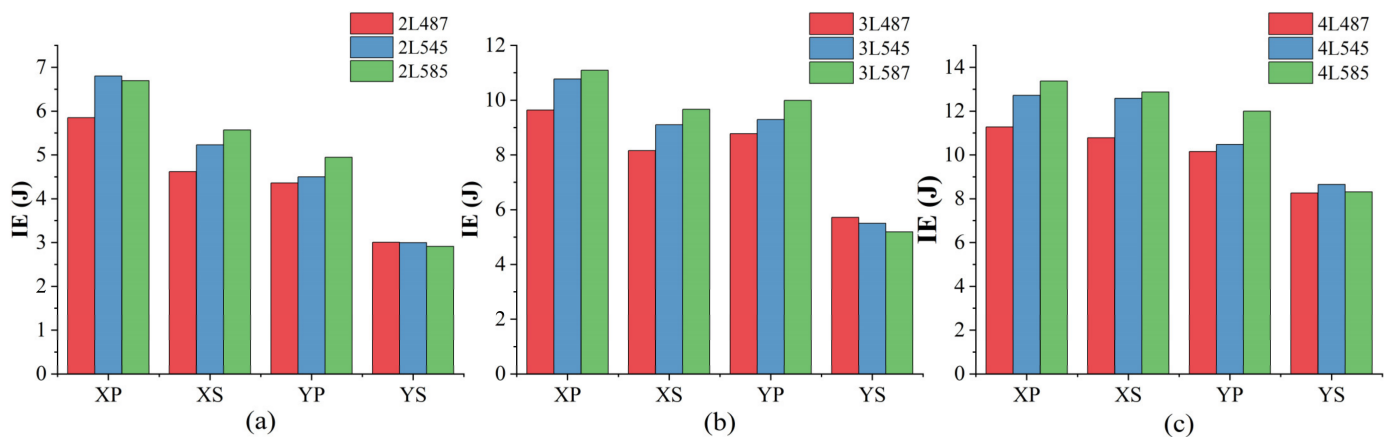

Figure 7. Internal energy absorption in primary and secondary yarns of (**a**) 2-layer, (**b**) 3-layer, and (**c**) 4-layer 3DOW.

The contours of yarn-level FEM damage illustrate the effect of x-yarn density on the impact response of 3DOW composites. Figure 8 shows the tensile and compressive damage distribution on the top and bottom surfaces of 2-layer 3DOW at 1 ms. SDV17 and SDV18 are the solution-dependent variables (SDV) used within VUMAT in ABAQUS to track additional outputs. In this study, SDV17 and SDV18 represent the compressive and tensile failure indices ranging from 0 to 1, respectively. The compressive damage contour on the upper surface of the 2-layer 3DOW models is compared in Figure 8a,c,e. The compressive damage area at the model's center decreases as the density of the x-yarn increases. The observed phenomenon can be attributed to the reduction in constraint between the y- and x-yarns, which is caused by a decrease in the number of x-yarns. As Figure 8 a,c,e suggest, this reduction in constraint increases the composite's susceptibility to compressive damage. The introduction of additional fibers during the impact event has been observed to result in a higher density of x-yarn, thereby restricting the extent of damage to the y-yarn orientation.

The distribution of tensile damage at the bottom layer of the 3DOW models is then investigated. The comparison of fiber tensile damage for 2-layer 3DOW with variable x-yarn densities is illustrated in Figure 8b,d,f. The results indicate that, at 1 ms, 2L587 exhibits the smallest amount of back face area subjected to fiber tensile damage, with 2L545 and 2L487 following in order of increasing magnitude. The results confirm that augmenting the density of x-yarns is an efficient measure to mitigate tensile damage of fibers located at the rear of the 3DOW with two layers in both the y- and x-directions.
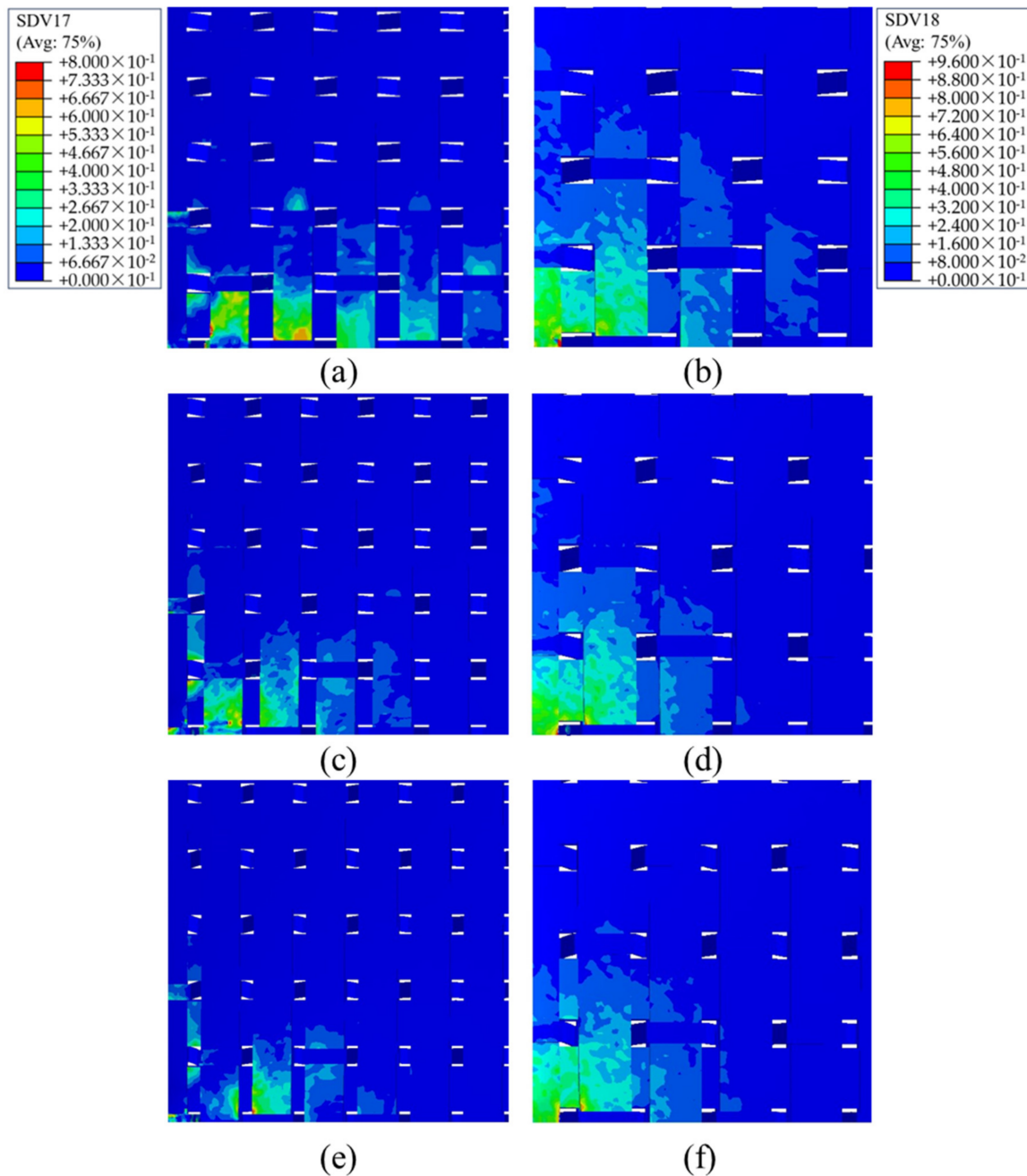
Figure 8. Damage contour of 2-layer 3DOW under 4.4 m/s impact at t = 1 ms: (**a**) face fiber compressive damage for 2L487; (**b**) back fiber tensile damage for 2L487; (**c**) face fiber compressive damage for 2L545; (**d**) back fiber tensile damage for 2L545; (**e**) face fiber compressive damage for 2L587; (**f**) back fiber tensile damage for 2L587.

Figure 9a–c illustrates the damaged backside of the 2-layer 3DOW models with varying x-yarn densities at different moments. At 0.9 ms, there is no significant variation in damage area between the three models (2L487, 2L545, and 2L587 in Figure 9). At 0.94 ms, however, cracks along the y-yarn direction begin to appear in all models, with 2L587 exhibiting a crack near the impact center. In 2L487, x-yarn direction cracks appear at 0.97ms, accompanied by a small y-yarn direction branch, whereas in 2L545, cracks propagate in both y- and x-directions. At the 0.99 ms and 1.01 ms marks, as shown in Figure 9a, the resin matrix of sample 2L487 displays a distinct "F" shape, with more damage in the y-yarn direction. A decreased x-yarn density results in less constraint between the y- and x-yarns, making the composite more susceptible to resin damage in the y-yarn direction. In contrast, model

2L545 exhibits an L-shaped resin damage pattern, as shown in Figure 9b, which is indicative of the improved yarn interlocking and load transmission between the y- and x-yarns as a result of the composite model's increased weave density. Consequently, these results in a proportional distribution of damage, with comparable levels of y- and x-direction resin damage. The resin damage on the 2L587 model, as illustrated in Figure 9c, is mainly aligned with the x-yarn direction. This suggests that under 219J of impact energy, the impact resistance of 2L587 is determined primarily by the x-yarns at this pick density. Consequently, a greater number of x-yarn density enhances yarn interlocking, promoting more efficient load transfer along the x-yarn direction, leading to predominantly x-directed localized damage.
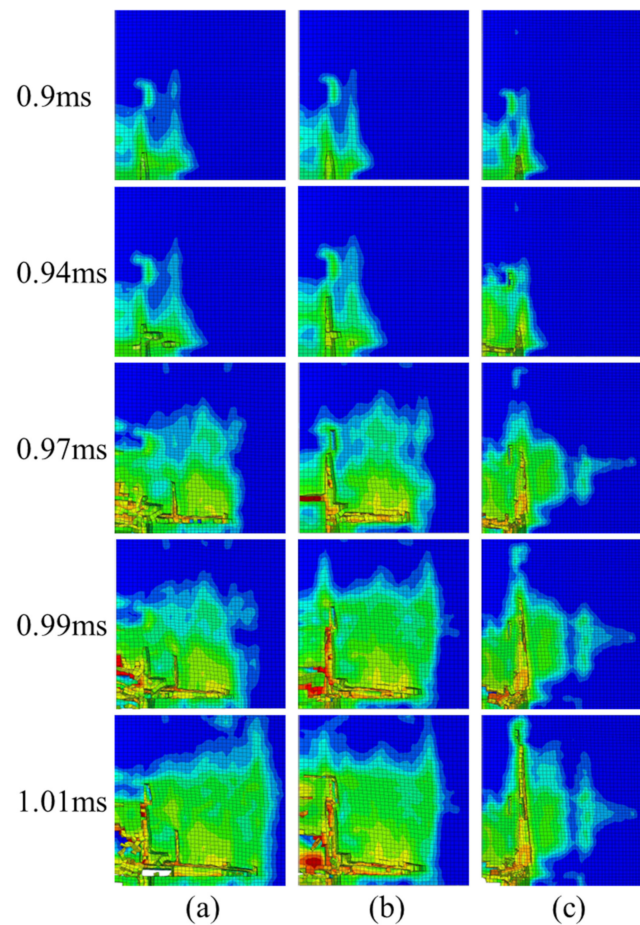

Figure 9. Damage propagation on back face of resin matrix for (**a**) 2L487, (**b**) 2L545, and (**c**) 2L587.

3.3. Effect of Binder Yarn Paths

Figure 10a illustrates the FEA energy absorption of 2-layer 3DOW models with plain, twill, and basket binder paths. The model with the plain binder path showcases the highest energy absorption, and the energy absorption is greater for the twill structure than for the basket structure. Figure 10b reveals a notable difference in the internal energy (IE) of the XP among the three variants. As shown in Figure 10a, the 2LPlain model has the maximum IE, placing it in the lead. The 2LTwill model is in second place, while the basket model is substantially behind, as it transfers much less energy to the IE in XP. The analysis of the IE absorption in warp primary yarns shows that the plain and basket models have a marginal advantage over the twill model. However, when studying the IE absorption in the weft primary yarns, both 2LPlain and 2LBasket models outperformed 2LTwill, showing similar levels of energy absorption. Finally, when comparing the warp secondary yarns, the secondary yarns of the 2LBasket model had more IE than those of the other two

models, and the remaining two models showed comparable levels of IE absorption in the secondary yarns.
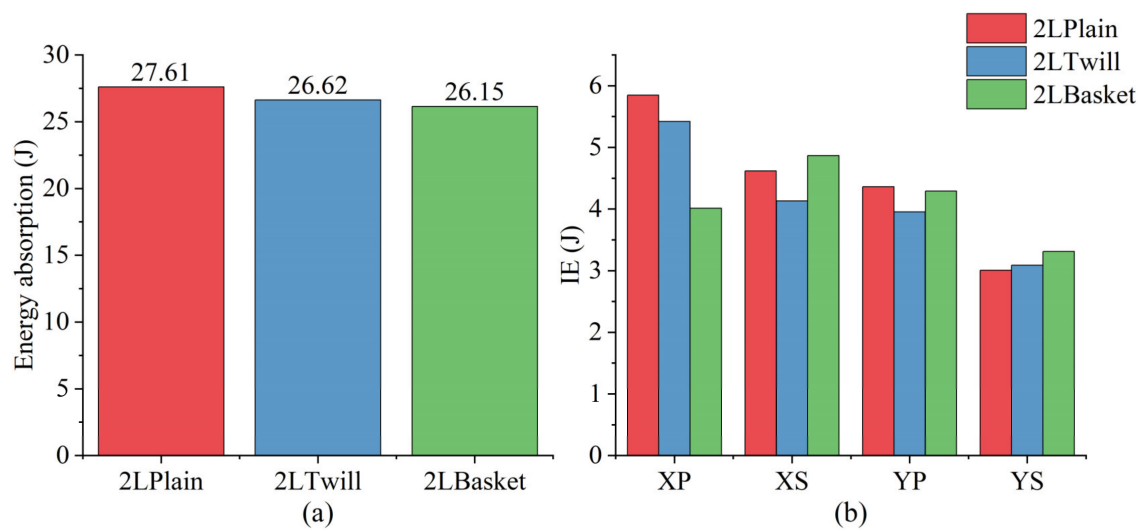

Figure 10. (**a**) Internal energy absorption of 2-layer 3DOW with different binder yarn paths, (**b**) internal energy distribution in primary and secondary yarns of 3DOW.

Figure 11 illustrates the positions of interlacement (yellow circles) between the binder yarn and x-yarn located at the top layer of the reinforcements in both plain and twill structures. However, due to the inherent characteristics of the basket weave, such interlacement does not exist in the basket structure at this position. The hypothesis is that this interlacing prevents the x-yarn from fully participating in the impact mitigation. This is due to the binder yarn present at the interlacement, which applies greater loads on the x-yarn from the upper side compared to the loads applied by the resin elements. The fiber material located on the right-hand side of the interlacement (yellow circles in Figure 11a–c) exhibits greater strength, thereby providing increased resistance to the x-yarn. The areas where the yarn breaks during impact are marked in red in Figure 11. The sites that have incurred damage on 2LPlain and 2LTwill, as illustrated in Figure 11a,b, are situated close to the point of impact. In contrast, the fractures of yarns observed in the basket model are located at a greater distance from the impact center as presented in Figure 11c. The lack of a cross-over between the binder yarn and x-yarn at the impact center of 2LTwill may cause further breakage on the third x-yarn. The second x-yarn from the center of the basket structure has experienced a fracture at the third interlacement with the z-yarn. The absence of interlacing between the x-yarn and the binder yarn at the cross-over point (highlighted by yellow circles in Figure 11), as opposed to the plain and twill weaves, results in a reduction of the loads applied from the upper side of the x-yarn. The lack of interlacement in the basket weave, which is inherent to the 2 × 2 basket structure, results in reduced engagement of the x-yarn during impact. As a result, the y-yarns are more significantly damaged, leading to the fracture of fibers at the third y-yarn located at the upper part of the 2LBasket, as illustrated by red rectangular in Figure 11c.

The propagation of damage on the back face of the resin matrix of 2-layer 3DOW with varying binder yarn paths is illustrated in Figure 12. The plain structure exhibits reduced damage along the x-yarn direction at 0.93 ms, as shown in Figure 12a. The propagation of the damage pattern in the y-yarn direction initiates in all models at 0.96 ms. The F-shaped resin damage pattern is observed in the resin matrix of 2LPlain at 0.99 ms, wherein the longer side is oriented along the y-yarn direction. Comparatively, lesser damage is observed in the x-yarn direction. At 1.02 ms, the center of impact of the plain structure was severely damaged, indicating a localized damage pattern.
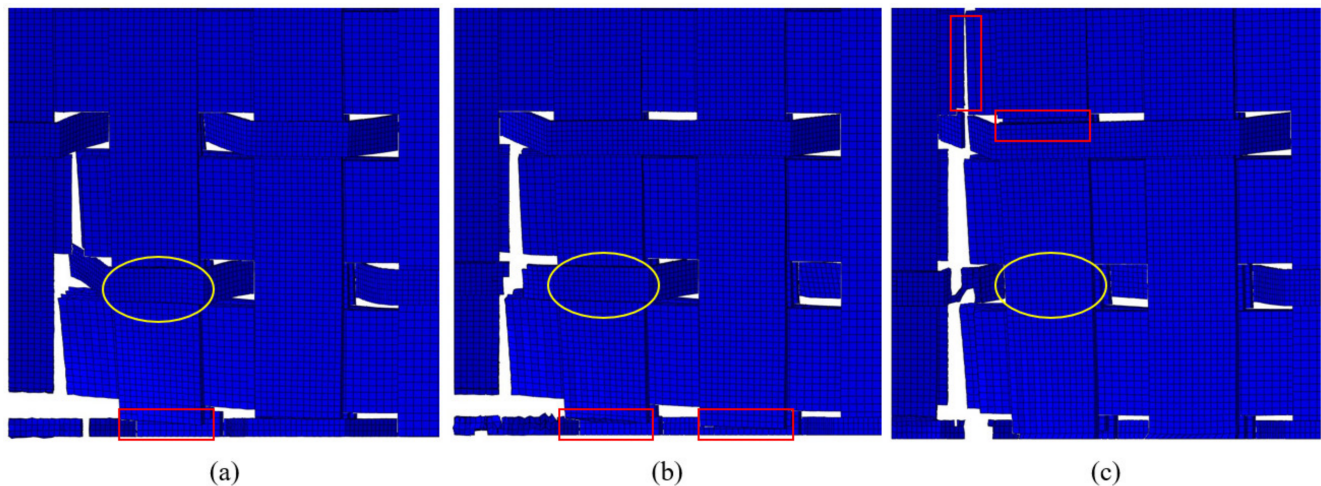
Figure 11. Yarn breakage locations in (**a**) 2LPlain, (**b**) 2LTwill, and (**c**) 2LBasket.

In contrast, the other two models (Figure 12b,c) exhibit a continued growth of damage via the y-yarn direction. The propagation of damage in 2LTwill (Figure 12b) is found to be more evident in the x-yarn direction, with significant damage being observed at the point of impact. For the basket weave structure, notable crack propagation is observed predominantly in the x-yarn direction, as illustrated in Figure 12c. Furthermore, there is no obvious sign of damage in the center region on the backside of the resin matrix. Among the three structures, it can be observed that 2LPlain exhibits the most restricted interlacement at the impact center. This results in a greater concentration of damage near the impact center, with x-yarn breakage being observed close to the point of impact. The presence of F-shaped resin damage on the back side of the plain composite model, as depicted in Figure 12a, suggests an increased stress concentration in the y-yarn direction. The observed L-shaped region, which exhibits similar length in the y-yarn direction, implies a uniform distribution of stress between the y- and x-yarns within the twill structure, as shown in Figure 12b. The present study reveals that the basket weave has fewer yarn cross-overs at the impact center compared to the plain and twill weaves. This reduces stress concentration at the cross-over points, allowing the crack to advance further along the x-yarn direction before encountering resistance from yarn interlacements, as demonstrated in Figure 12c. Furthermore, the increased size of the unit cells within the basket weave configuration affords greater flexibility and capacity for deformation in the composite material. The structure exhibits greater deformability and less localized damage in the center when exposed to an impact. Due to the larger unit cells and looser interlacing, the load can be distributed over a larger area, which contributes to the crack propagating deeper into the x-yarn direction in the basket weave.
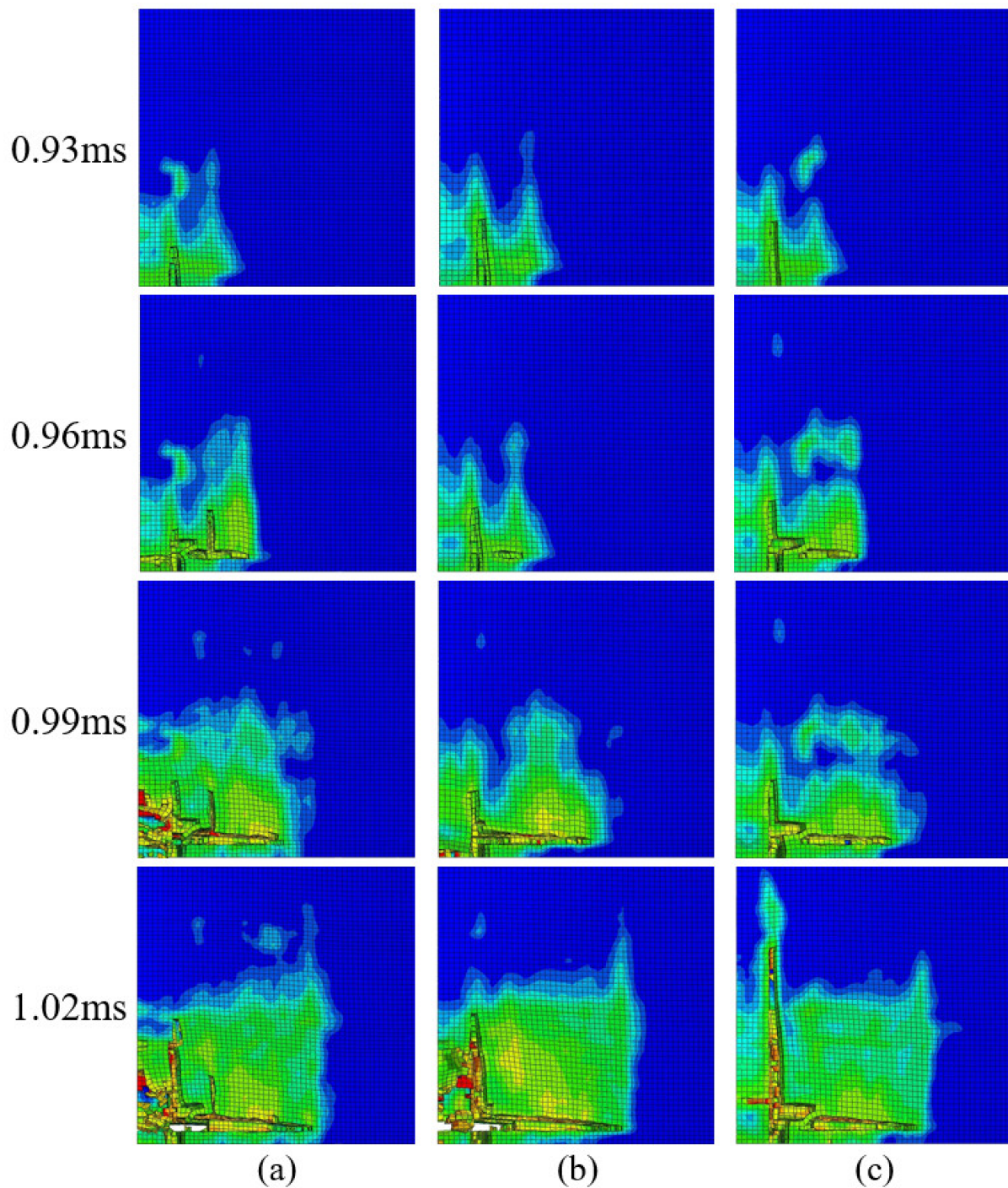
Figure 12. Damage propagation on back face of resin matrix for (**a**) 2LPlain, (**b**) 2LTwill, and (**c**) 2LBasket.

4. Conclusions

The primary objective of this study was to use the finite element method to investigate the effects of x-yarn densities and binder yarn paths on the impact resistance of 3D orthogonal woven composites. Based on the measured geometric parameters, yarn-level FE models were developed and validated. As the x-yarn density increased from 4.87 picks/cm to 5.87 picks/cm, the average energy absorption of 2-, 3-, and 4-layer 3DOW models increased by 15.18%, 11.45%, and 15.6%, respectively. The increase in total energy absorption due to increasing x-yarn density in 3DOW composites is mainly attributed to the improved internal energy absorption.

An increase in the number of x-yarns in 3DOW models led to reduced fiber tensile damage on the back face and fiber compressive damage on the front side. Moreover, the morphology of cracks observed in the back of the composite changed with x-yarn density. Cracks observed on the model with the lowest x-yarn density predominantly extended in the y-yarn direction, while increasing x-yarn density shifted the damage to the resin matrix along the x-yarn direction, suggesting reduced vulnerability in the y-direction.

The study of different binder yarn paths shows that they have a unique effect on the impact resistance of 3DOW composites in both energy absorption and damage morphology. The primary weft yarns in the basket model absorbed less internal energy than the counterparts, while its secondary yarns absorbed more. Moreover, the reduced number of interlacements between the binder yarn and x-yarn in the basket model resulted in the decreased engagement of the x-yarn during impact, which resulted in altered crack extension in the resin matrix.

This study exemplifies the applicability of using validated finite element models to predict the effects of various structural parameters on the impact response of 3DOW composites. It enhances the understanding of how these structural parameters influence the performance of 3DOW composites under impact. The study provides valuable insights that can inform the design and optimization of complex woven structures. Future work should focus on changing the impact locations in 3DOW composites to further optimize the performance of 3DOW composites.

Author Contributions: Conceptualization, A.-F.M.S.; methodology, A.-F.M.S., W.X. and M.Z.; software, W.X.; validation, A.-F.M.S., W.X. and M.Z.; investigation, A.-F.M.S., W.X. and M.Z.; resources, A.-F.M.S.; data curation, W.X.; writing—original draft preparation, W.X.; writing—review and editing, A.-F.M.S. and M.Z.; visualization, W.X.; supervision, A.-F.M.S. and M.Z.; project administration, A.-F.M.S. and M.Z.; funding acquisition, A.-F.M.S. All authors have read and agreed to the published version of the manuscript.

Data Availability Statement: The data are available upon request.

Conflicts of Interest: The authors declare no conflicts of interest.

References

1. Huang, T.; Wang, Y.; Wang, G. Review of the Mechanical Properties of a 3D Woven Composite and Its Applications. *Polym. Plast. Technol. Eng.* **2018**, *57*, 740–756. [CrossRef]
2. Abtew, M.A. A comprehensive review on advancements, innovations and applications of 3D warp interlock fabrics and its composite materials. *Compos. B Eng.* **2024**, *278*, 111395. [CrossRef]
3. Wen, F.; Qian, Y.; Gao, Y.; Zhou, X.; Lyu, L. 3D woven tubular composites with bamboo-structures for enhanced energy absorption: Designing, manufacturing and performance analysis. *Polym. Compos.* **2024**. [CrossRef]
4. Mouritz, A.P. Review of z-pinned composite laminates. *Compos. Part. A Appl. Sci. Manuf.* **2007**, *38*, 2383–2397. [CrossRef]
5. Seltzer, R.; González, C.; Muñoz, R.; Llorca, J.; Blanco-Varela, T. X-ray microtomography analysis of the damage micromechanisms in 3D woven composites under low-velocity impact. *Compos. Part. A Appl. Sci. Manuf.* **2013**, *45*, 49–60. [CrossRef]
6. Hart, K.R.; Chia, P.X.L.; Sheridan, L.E.; Wetzel, E.D.; Sottos, N.R.; White, S.R. Mechanisms and characterization of impact damage in 2D and 3D woven fiber-reinforced composites. *Compos. Part. A Appl. Sci. Manuf.* **2017**, *101*, 432–443. [CrossRef]
7. Xuan, J.Q.; Li, D.S.; Jiang, L. Fabrication, properties and failure of 3D stitched carbon/epoxy composites with no stitching fibers damage. *Compos. Struct.* **2019**, *220*, 602–607. [CrossRef]
8. Bogdanovich, A.E.; Singletary, J.N. Ballistic performance and applications of 3-D woven fabrics and composites. In Proceedings of the 9th European Conference on Composite Materials, ECCM9, Brighton, UK, 4–7 June 2000.
9. Bilisik, K.; Karaduman, N.S.; Bilisik, N.E.; Bilisik, H.E. Three-dimensional fully interlaced woven preforms for composites. *Text. Res. J.* **2013**, *83*, 2060–2084. [CrossRef]
10. Dewangan, M.K.; Panigrahi, S.K. Finite element analysis of hybrid 3D orthogonal woven composite subjected to ballistic impact with multi-scale modeling. *Polym. Adv. Technol.* **2021**, *32*, 964–979. [CrossRef]
11. Dewangan, M.K.; Panigrahi, S.K. Multiscale Modelling of 3D Orthogonal Woven Composite under Ballistic Impact Using FEM. *Fibers Polym.* **2020**, *21*, 2389–2400. [CrossRef]
12. Sharp, K.; Bogdanovich, A.; Boyle, R.; Brown, J.; Mungalov, D. Wind blade joints based on non-crimp 3D orthogonal woven Pi shaped preforms. *Compos. Part. A Appl. Sci. Manuf.* **2013**, *49*, 9–17. [CrossRef]

13. Karahan, M.; Lomov, S.V.; Bogdanovich, A.E.; Mungalov, D.; Verpoest, I. Internal geometry evaluation of non-crimp 3D orthogonal woven carbon fabric composite. *In Compos. Part. A Appl. Sci. Manuf.* **2010**, *41*, 1301–1311. [CrossRef]
14. Carvelli, V.; Pazmino, J.; Lomov, S.V.; Verpoest, I. Deformability of a non-crimp 3D orthogonal weave E-glass composite reinforcement. *Compos. Sci. Technol.* **2012**, *73*, 9–18. [CrossRef]
15. Miao, H.; Wu, Z.; Ying, Z.; Hu, X. The numerical and experimental investigation on low-velocity impact response of composite panels: Effect of fabric architecture. *Compos. Struct.* **2019**, *227*, 111343. [CrossRef]
16. Wu, Z.; Zhang, L.; Ying, Z.; Ke, J.; Hu, X. Low-velocity impact performance of hybrid 3D carbon/glass woven orthogonal composite: Experiment and simulation. *Compos. B Eng.* **2020**, *196*, 108098. [CrossRef]
17. Saleh, M.N.; Yudhanto, A.; Potluri, P.; Lubineau, G.; Soutis, C. Characterising the loading direction sensitivity of 3D woven composites: Effect of z-binder architecture. *Compos. Part. A Appl. Sci. Manuf.* **2016**, *90*, 577–588. [CrossRef]
18. Hu, X.; Ying, Z.; Cheng, X.; Wu, Z. Effect of Z-binder tension and internal micro-structure on damage behavior of 3D orthogonal woven composite. *J. Ind. Text.* **2019**, *49*, 551–571. [CrossRef]
19. Zhang, F.; Liu, K.; Wan, Y.; Jin, L.; Gu, B.; Sun, B. Experimental and numerical analyses of the mechanical behaviors of three-dimensional orthogonal woven composites under compressive loadings with different strain rates. *Int. J. Damage Mech.* **2014**, *23*, 636–660. [CrossRef]
20. Luo, Y.; Lv, L.; Sun, B.; Qiu, Y.; Gu, B. Transverse impact behavior and energy absorption of three-dimensional orthogonal hybrid woven composites. *Compos. Struct.* **2007**, *81*, 202–209. [CrossRef]
21. Baucom, J.N.; Zikry, M.A. Low-velocity impact damage progression in woven E-glass composite systems. *Compos. Part. A Appl. Sci. Manuf.* **2005**, *36*, 658–664. [CrossRef]
22. Baucom, J.N.; Zikry, M.A. Evolution of Failure Mechanisms in 2D and 3D Woven Composite Systems Under Quasi-Static Perforation. *J. Compos. Mater.* **2003**, *37*, 1651–1674. [CrossRef]
23. Castaneda, N.; Wisner, B.; Cuadra, J.; Amini, S.; Kontsos, A. Investigation of the Z-binder role in progressive damage of 3D woven composites. *Compos. Part. A Appl. Sci. Manuf.* **2017**, *98*, 76–89. [CrossRef]
24. Hart, K.R.; Chia, P.X.L.; Sheridan, L.E.; Wetzel, E.D.; Sottos, N.R.; White, S.R. Comparison of Compression-After-Impact and Flexure-After-Impact protocols for 2D and 3D woven fiber-reinforced composites. *Compos. Part. A Appl. Sci. Manuf.* **2017**, *101*, 471–479. [CrossRef]
25. Midani, M.; Seyam, A.-F.; Saleh, M.N.; Pankow, M. The effect of the through-thickness yarn component on the in- and out-of-plane properties of composites from 3D orthogonal woven preforms. *J. Text. Inst.* **2019**, *110*, 317–327. [CrossRef]
26. Ghosh, R.; De, S. Z-fiber influence on high speed penetration of 3D orthogonal woven fiber composites. *Mech. Mater.* **2014**, *68*, 147–163. [CrossRef]
27. Dai, S.; Cunningham, P.R.; Marshall, S.; Silva, C. Influence of fibre architecture on the tensile, compressive and flexural behaviour of 3D woven composites. *Compos. Part. A Appl. Sci. Manuf.* **2015**, *69*, 195–207. [CrossRef]
28. Kumar, A.; Bijoya, D.; Behera, K.; Dash, A.K.; Behera, B.K. Role of weave design on the mechanical properties of 3D woven fabrics as reinforcements for structural composites. *J. Text. Inst.* **2017**, *109*, 952–960.
29. Sun, J.; Dai, Y.; Huang, L.; Zhang, D.; Zhao, J. Micromechanisms and Characterization of Low-Velocity Impact Damage in 3D Woven Composites. *Materials* **2022**, *15*, 6636. [CrossRef]
30. Nasrun, F.M.Z.; Yahya, M.F.; Ghani, S.A.; Ahmad, M.R. Effect of weft density and yarn crimps towards tensile strength of 3D angle interlock woven fabric. *AIP Conf. Proc.* **2016**, *1774*, 020003.
31. Li, Z.; Li, D.; Zhu, H.; Guo, Z.; Jiang, L. Mechanical properties prediction of 3D angle-interlock woven composites by finite element modeling method. *Mater. Today Commun.* **2020**, *22*, 100769. [CrossRef]
32. Hamouda, T.; Seyam, A.F.M.; Peters, K. Evaluation of the integrity of 3D orthogonal woven composites with embedded polymer optical fibers. *Compos. B Eng.* **2015**, *78*, 79–85. [CrossRef]
33. Neale, G.; Dahale, M.; Yoo, S.; Toso, N.; McGarrigle, C.; Quinn, J.; Kelly, J.; McIlhagger, A.; Archer, E.; Harkin-Jones, E. Improved crush energy absorption in 3D woven composites by pick density modification. *Compos. B Eng.* **2020**, *192*, 108007. [CrossRef]
34. Midani, M.; Seyam, A.F.; Pankow, M. The Effect of the Structural Parameters of 3D Orthogonal Woven Composites on their Impact Responses under Different Modes of Impact. *Key Eng. Mater.* **2018**, *786*, 215–223. [CrossRef]
35. Haque, B.Z.G. A progressive composite damage model for unidirectional and woven fabric composites. *MAT162 User Man.* **2015**, *10*.
36. Tabatabaei, S.A.; Lomov, S.V.; Verpoest, I. Assessment of embedded element technique in meso-FE modelling of fibre reinforced composites. *Compos. Struct.* **2014**, *107*, 436–446. [CrossRef]
37. Gama, B.A.; Gillespie, J.W. Finite element modeling of impact, damage evolution and penetration of thick-section composites. *Int. J. Impact Eng.* **2011**, *38*, 181–197. [CrossRef]
38. Xiao, J.R.; Gama, B.A.; Gillespie, J.W. Progressive damage and delamination in plain weave S-2 glass/SC-15 composites under quasi-static punch-shear loading. *Compos. Struct.* **2007**, *78*, 182–196. [CrossRef]
39. Hazzard, M.K.; Trask, R.S.; Heisserer, U.; Van Der Kamp, M.; Hallett, S.R. Finite element modelling of Dyneema®composites: From quasi-static rates to ballistic impact. *Compos. Part. A Appl. Sci. Manuf.* **2018**, *115*, 31–45. [CrossRef]
40. Yuan, Z.; Ma, W.; Xu, W.; Sun, Y.; Gu, B.; Chen, X. A numerical study on stress wave propagation in quasi-isotropic stacks of Dyneema®compliant composite laminates. *Compos. Struct.* **2023**, *312*, 116869. [CrossRef]

41. Sridharan, S.; Pankow, M. Performance evaluation of two progressive damage models for composite laminates under various speed impact loading. *Int. J. Impact Eng.* **2020**, *143*, 103615. [CrossRef]

42. Jia, X.; Sun, B.; Gu, B. Ballistic penetration of conically cylindrical steel projectile into 3D orthogonal woven composite: A finite element study at microstructure level. *J. Compos. Mater.* **2011**, *45*, 965–987.

43. Gama, B.A.; Bogetti, T.A.; Gillespie, J.W., Jr. Progressive Damage Modeling of Plain-Weave Composites using LS-Dyna Composite Damage Model MAT162. In Proceedings of the 7th European LS-DYNA Conference, Salzburg, Austria, 14–15 May 2009.

44. Hausrath, R.L.; Longobardo, A.V. High-strength glass fibers and markets. *Fiberglass Glass Technol. Energy-Friendly Compos. Appl.* **2010**, 197–225.

45. Cheeseman, B.A.; Bogetti, T.A. Ballistic impact into fabric and compliant composite laminates. *Compos. Struct.* **2003**, *61*, 161–173. [CrossRef]

46. Abaqus 2016 Documentation. Available online: http://130.149.89.49:2080/v2016/index.html (accessed on 20 September 2019).